Thermal Enhancement of Product Conductivity Permits Deep Discharge in Solid State Li-O_2 Batteries

Alexander A. Delluva[a,b], Jonas Kulberg-Savercool[a], Adam Holewinski*,[a,b,c]

[a]*Department of Chemical and Biological Engineering. University of Colorado, Boulder, CO 80309.* [b]*Renewable and Sustainable Energy Institute. University of Colorado, Boulder, CO 80309.* [c]*Materials Science and Engineering Program. University of Colorado, Boulder, CO 80309.*

*Corresponding author email: adam.holewinski@colorado.edu

Abstract

Li-O_2 batteries are mainly limited by the poor conductivity of their discharge products as well as parasitic reactions with carbon-containing electrodes and electrolytes. Here, Li-O_2 cells utilizing inorganic solid state electrolytes are investigated as a means to operate at elevated temperature, thereby increasing the conductivity of discharge products. Growth of dense, conductive Li_xO_y products further removes the need for high surface area support structures commonly made of carbon. Patterned Au electrodes, evaporated onto $Li_7La_3Zr_2O_{12}$ (LLZO) solid electrolyte, are used to create a triple phase boundary for the nucleation of discharge product, with growth outward into the cell headspace with gaseous O_2. Through capacity measurements and imaging, discharge product growths are estimated to reach a critical dimension of approximately 10 microns, far exceeding what would be possible for a conformal film based on its room temperature electronic conductivity. Raman spectroscopy and electrochemical mass spectrometry (EC-MS) are used to characterize the discharge chemistry and reveal a mixed lithium oxide character, with evidence of trace lithium hydroxides and initial carbonate contamination. These results showcase that thermal enhancement of Li-O_2 batteries could be a viable strategy to increase capacity when paired with solid electrolytes.

1. Introduction

Li-O_2 batteries have been widely investigated due to their theoretical energy density being among the highest possible for different battery chemistries.[1,2] However, parasitic reactions, poor cycling stability, and the insulating nature of their discharge products—mainly Li_2O_2—have all proven to be large hurdles for the practical implementation and commercialization of these cells.[3-8] Two primary pathways forming Li_2O_2 have been identified in conventional liquid aprotic electrolyte Li-O_2 cells. These are commonly referred to as surface-mediated and solution-mediated mechanisms.[9] The former proceeds by sustained growth of a film on the cathode surface until a limiting thickness is reached. The overpotential grows rapidly as a function of thickness due to conductivity limitations of Li_2O_2 and thus results in the so-called "sudden death" of the cell, severely limiting the realized capacity.[10,11] In contrast, the solution mechanism circumvents the conductivity limitation by moving the insulating Li_2O_2 products out of the conduction path of electrons. It relies on the dissolution of the surface intermediate LiO_2, which can disproportionate and deposit large particulate Li_2O_2 without covering the cathode surface.[12–14] While this mechanism can therefore result in a marked increase in cell capacity due to thicker discharge products, detachment of these particles from the electrode[15] and parasitic reactions from organic electrolytes[8,16] are still issues in these cells, ultimately limiting their cycle life.

In the present contribution we investigate a novel solid state electrolyte (SSE)-based architecture for Li-O_2 that could offer two significant benefits when compared to typical liquid electrolyte cells: (i) access to much higher operating temperatures promotes depth of discharge through thermal-enhancement of ionic and electronic conductivities of the discharge product, and (ii) the absence of carbon—in either electrolyte or electrode—circumvents the parasitic reactions commonly found with organic electrolytes and graphitic electrodes. Additionally, because

discharge products in solid state Li-O_2 (SSLO) batteries grow into the gaseous cell headspace rather than a liquid electrolyte, limitations due to O_2 solubility and transport are not expected. It may be noted that elevated operating temperatures have been previously employed in Li-O_2 batteries through the use of molten salt electrolytes, which have been found to largely mitigate parasitic solvent reactions.[15,17,18] Molten salts can also facilitate the solution mechanism, giving them a high depth of discharge (capacities up to 12 mAh/cm^2 reported),[18] but making them vulnerable to capacity fade via discharge product solubility and detachment. It is also worth noting that a change in the primary discharge product phase, from Li_2O_2 to Li_2O, has been observed above 150˚C.[17,18] For reference, the respective discharge reactions are:

$$1)\ 2\,Li^+ + O_2 + 2\,e^- \rightarrow Li_2O_2 \quad (E° = 2.82\ \text{V})$$

$$2)\ 2\,Li^+ + \frac{1}{2}O_2 + 2\,e^- \rightarrow Li_2O \ (E° = 2.82\ \text{V})$$

To our knowledge, there exist two demonstrations of solid state Li-O_2 cells utilizing elevated temperatures (120˚C[19] and 200˚C[20] respectively). However, both utilized carbon-containing cathodes, which can corrode and/or lead to formation of lithium carbonates, making the systems less well-suited for directly probing high temperature Li-O_2 chemistry and the possible gains associated with the increases in the conductivity of discharge products.

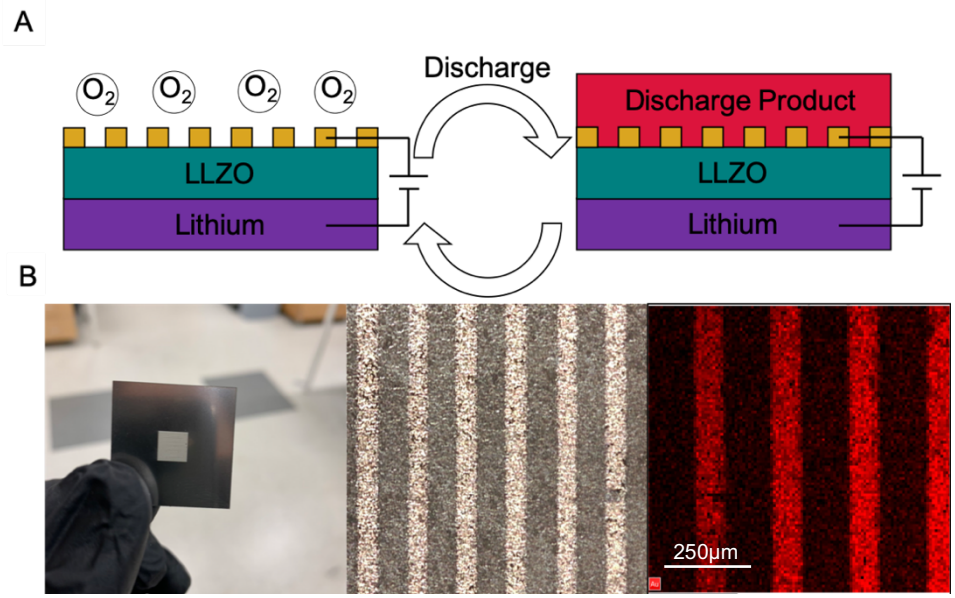

Figure 1. (A) Schematic view of cell architecture used in this study, portraying the formation and decomposition of discharge product during cell cycling. (B) Left: Photograph of mask, Center: optical microscopy image of patterned Au electrode atop LLZO pellet Right: SEM-EDS map of gold

Here, the proposed cell architecture involves a ceramic solid electrolyte, upon which a patterned metallic (Au) current collector is placed to permit lateral electron transport across the full cathode area (**Figure 1**). After initial nucleation at the LLZO-Au-O_2 triple-phase-boundary (TPB), sustained growth of the discharge can continue via conduction of electrons through the discharge product itself until a conductivity-limited thickness is achieved. By employing an SSE, the design promotes depth of discharge by permitting access to the much higher ionic and electronic conductivities of the discharge product at high temperatures. Conductivity data for discharge products (**Table 1**) indicate that Li_2O_2 and Li_2O show roughly two orders of magnitude increase between room temperature and 170°C (just below the melting temperature of Li). Additionally, the absence of organic materials helps to mitigate capacity-loss-inducing parasitic reactions. The cell architecture is similar to cells recently devised for studying the chemistry of

discharge products,[21–23] but we emphasize the fundamentally different motivation and usage here in attempting to engineer sustained growth of discharge products through a surface film mixed-conduction mechanism. Herein, we fabricate proof-of-concept cells and confirm the formation of discharge products by scanning election microscopy (SEM) and Raman spectroscopy. Galvanostatic charging and discharging measurements demonstrate a break-in period due to Li_2CO_3 contaminant decomposition, followed by stable long-term cycling. Electrochemical mass spectrometry (EC-MS) is further utilized in combination with electrochemical impedance spectroscopy (EIS) to better understand the nature and growth dynamics of the discharge products. This work provides proof of concept evidence that the hypothesized discharge mechanism and enhancement of limiting thicknesses are possible, and that higher energy densities should be achievable through finer current collector patterning.

Table 1. Conductivity data for Li_2O and Li_2O_2.[a]

	σ_{ion} (S/cm)			σ_{elec} (S/cm)			Reference
	25°C	170°C	Ea (eV)	25°C	170°C	Ea (eV)	
Li2O2 (exp)	1.7×10^{-12}	2.8×10^{-7}	0.95	5.1×10^{-16}	9.5×10^{-9}	1.3	24
Li2O (exp)	1.0×10^{-12}	3.9×10^{-8}	0.86	1.0×10^{-14}	3.9×10^{-10}	0.86[b]	25
a-Li2O2 (exp)	7.1×10^{-8}			5.02×10^{-9}			26
c-Li2O2 (calc)	1.4×10^{-18}	1.4×10^{-16}	0.36	2.2×10^{-19}	4.7×10^{-17}	0.42	27
a-Li2O2 (theo)	1.4×10^{-6}	1.5×10^{-3}	0.55[c]	9.3×10^{-15}	8.8×10^{-9}	1.08[c]	28

[a]Conductivities adjusted to 25°C and 170°C using an Arrhenius relationship with measured (experimental references) or computed (computational references) values of activation barrier. All surveyed experimental references had variation in control over crystallinity and concentration of extrinsic defects, so values are only meant to illustrate trends. [b]Barrier valid below 500 K. σ_{elec} only estimated in Ref. 25 to be 2 orders of magnitude smaller than σ_{ion}. [c]Barriers for amorphous materials in Ref 28 computed by threshold for a percolating network of defects.

2. Materials and Methods

2.1 Electrolyte Preparation

$Li_{6.4}La_3Zr_{1.4}Ta0.6O_{12}$ (LLZTO) was purchased from MTI Corporation (μ_d = 5 μm) and pelletized in a 13 mm stainless steel die (Across International) at 2 metric tons of pressure using a mechanical press (Carver Model M). The resulting pellets were placed in MgO boats within a tube furnace (Thermcraft® XST-3-0-36-1V2-F01) for a two-step sintering process[29], which has been shown to help densify pellets while limiting lithium loss through an initial high temperature nucleation step and then lower temperature grain growth. Pellets were initially heated to 1200˚C at a ramp rate of 3˚C/min and held for 1 hour. The temperature was then reduced to 1100˚C and held for 5 hours before cooling to room temperature at a rate of 100˚C/hr. The approximate density of the pellets was 90%. Faces of the pellets were polished in air progressively with 150, 400, 800, and 1000 grit sandpapers (3M®, proprietary ceramic), followed by wet polishing with 1, 0.3, and 0.05 μm alumina particles (Electron Microscopy Sciences) to ensure a flat surface for electrode deposition as well as to reduce Li_2CO_3 contamination that can re-form on the surface after calcination.[30] Pellets were then immediately transferred into an argon filled glovebox and heated to 400°C for 3 hours to remove residual Li_2CO_3.

2.2 Cathode Deposition

Pellets were affixed to shadow masks with a 6 mm x 6 mm square electrode area. The masked pellets were transferred under argon to a thermal evaporation chamber built within a nitrogen-filled glovebox (Angstrom Engineering). Gold (Kurt J. Lesker Company) was then evaporated in a two-step deposition process to a thickness of 200 nm (**Figure 1B**). The estimated elapsed time between carbonate removal and cathode deposition was 30 minutes. The gold patterned pellets were transferred under nitrogen back to the original glovebox and annealed at

200˚C to improve adhesion of the evaporated films. Silver conductive paste was spread across one edge of the patterned electrode to conductively link the patterned features.

2.3 Cell Assembly

(MBRAUN® Unilab Pro SP). To create the full cells, lithium foils were punched (10 mm diameter), scraped to remove oxide, pressed onto the LLZO pellet, and placed into customized Swagelok® cells. The side of the LLZO pellet opposite the Au was gently polished with 2000 grit sandpaper inside the glovebox prior to cell assembly to re-clean the interface before the adhesion of a scraped lithium foil to act as the cell anode. Porous stainless-steel discs (McMaster-Carr) were used as current collectors on both sides of the pellet stack. These stacks were placed within PEEK cells, clamped in a vice to apply stack pressure, and rapidly connected to the MS for electrochemical testing. All electrochemical measurements were performed on a Bio-logic SP-300 potentiostat/galvanostat/FRA.

2.4 Materials Characterization

SEM images were obtained on an FEI Nova 600 Nanolab (Dual Beam). Raman spectroscopy measurements were obtained on a Horiba LabRAM HR Evolution Spectrometer. Mass spectrometry measurements were performed using an HPR-40 DEMS (Hiden Analytical). All electrochemical measurements were performed on a Bio-logic SP-300 potentiostat/galvanostat/FRA.

3. Results and Discussion

3.1 Cycling Behavior and Product Characterization

To identify the redox features associated with molecular oxygen in SSLO cells, we first performed headspace composition switching experiments while monitoring the open circuit voltage (OCV). The OCV was measured upon initiating flow of argon through the cell, and the

final voltage (after complete purging of air) in this regime is consistent with an alloying reaction between lithium and the gold current collector. The cathode potential in the presence of O_2 (c.f. Eqs. 1-2) is much higher than the standard potential for this alloying process (~1.6 V vs. Li/Li^+)[31], so it is not expected to be relevant during actual operation. Regardless, it is not a significant capacity contribution. Upon subsequent switching to oxygen flow through the cell, a large increase in the OCV was observed (**Figure 2A**), corresponding to the presence of Li-O_2 redox behavior. A first half-cycle discharge voltage profile for these cells (**Figure 2B)** shows a sharp drop to 2.4 V, followed by a steady decay down to 2 V, consistent with the formation of an increasingly insulating discharge product on the cell cathode. To further probe the redox behavior during the startup phase, a series of cyclic voltammograms (CVs) was run under argon and oxygen. The first CV cycle under argon (**Figure S1A**) showed several peaks related to air exposure during cell assembly/transport, disappearing on a second cycle (**Figure S1B**). Introduction of O_2 to this cell caused several of these initial peaks to reappear, and we thus attribute these to the formation and decomposition of Li-O_2 discharge products. The nature of these peaks will be discussed in the context of stable cycling further below.

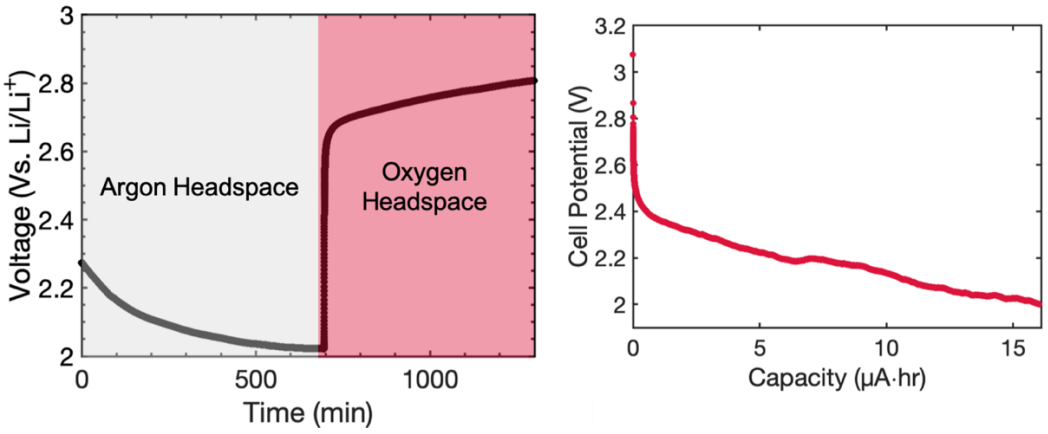

Figure 2. (A) Measured OCV of cell at 170℃ before and after introduction of O_2 into the headspace. Initial voltage drift under Ar is associated with purging of air from the cell. (B) First cycle discharge curve of Li_xO_y | Au | LLZO | Li cell.

Figure 3A shows an SEM image of the cathode surface after discharge. During discharge, product is deposited at the triple-phase boundary between the LLZO, Au, and O_2 headspace, which can be seen along the edges of the gold current collector. We obtain estimates of the thickness of discharge to be ~10 microns from these images, by looking at the lateral growth of the film outward from the gold current collector. We emphasize that the current collector patterning is far from optimized—in other words, we suggest that it should be possible to grow a *complete* overlayer of product to similar thickness using much finer current collector grids. Raman spectroscopy (**Figure 3B**) measurements identify the appearance of Li_2O_2 (peaks at 790, 810, and 920 cm^{-1}) and Li_2O (540 cm^{-1}), not present on the clean LLZO surface. (A summary of Raman peaks for commonly observed lithium compounds is presented in Table S1 for reference). Li_2CO_3 is also observed, but this is likely an artifact from air exposure of LLZO during transfer to the Raman instrument—carbonates are rapidly decomposed during early cycling (*vide infra*). A Raman peak tentatively assigned to LiO_2 was also detected at 1120 cm^{-1}, although it should be noted that the identification of purported LiO_2 signatures has been a subject of debate as this species is not stable.[32,33] While LiO_2 has never been isolated, it has been argued to be kinetically stable in some organic solvents.[34] Assignment on solid state surfaces is even less established, although typical interferences that can come from solvents and binders are not present in the SSE system (no precursors are organic and the LLZO is calcined at 1200°C). Superoxide-like species have been argued to exist previously on gold electrodes[34]—in the absence of these binders as well—and we thus suggest that the peak at 1120 cm^{-1} is true Li-superoxide. The peak at 675 cm^{-1} is currently unidentified; however, we suspect it could be related to a partially hydrated discharge product, as will be discussed further below.

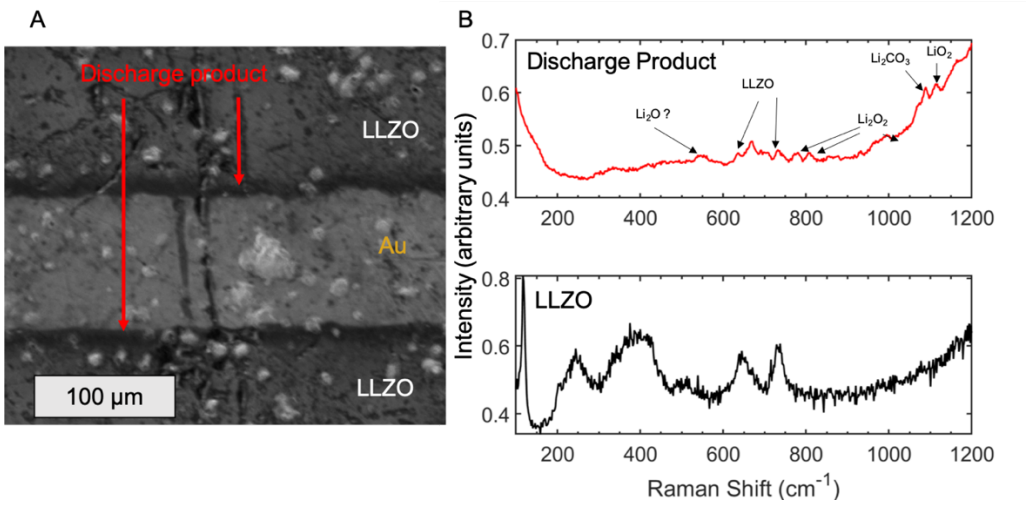

Figure 3. (A) SEM image of discharged electrodes after cycling (scale bar 100 µm). (B) Raman spectra of LLZO (red) and discharge product formed above LLZO (black).

Galvanostatic cycling was next performed to understand the time evolution and stability of the discharge processes. Before reaching stable cycling behavior, the first cycle in each experiment was found to yield a much larger discharge capacity than could be recharged or observed on the second cycle (initial coulombic efficiency ~300%, defined by ratio of discharge capacity to subsequent charge capacity). This can be attributed to the decomposition of contaminant phases including Li_2CO_3 and LiOH. After this first cycle, a more stable performance was established, with coulombic efficiencies near to 100% on each cycle. Cycling was characterized at two temperatures, 170˚C (**Figure 4A**) and 100˚C (**Figure S2**). Greater than an order of magnitude increase in the capacity (at any given cycle) was observed for the higher temperature cells—a change that can be attributed to increased conductivity of the discharge product. Doubling the rate of cycling (for example, initial step from 1µA to 2µA over cycles 7-13 in the figure) resulted in lower capacity; however, the original higher capacity was recoverable upon returning to lower cycling current. More interestingly, it was further observed that cell capacities tended to slowly increase over the course of early cycling (origins to be discussed further below), and, due to the increasing capacity,

we employed an accelerated cycling procedure with periodic increases to the current density. For the cell in Figure 4, the growth was found to continue for many dozens of cycles with no sign of leveling off, so the current was increased to 2μA after 55 cycles—after which the pattern of capacity growth was still observed—and then further increased to 10 μA from the 100 cycle mark onward. This final increase apparently represented a sufficiently high rate that sources of capacity loss outpace those leading to gain, and the capacity faded considerably over 50 additional cycles until cell failure. This general behavior was reproducible on a several similarly-fabricated cells.

Based on the observed capacity growth phenomenon, we suggest that the general tendency for deviations above 100% coulombic efficiency may be due to incomplete decomposition of discharged products. The Li foil anode represents an effectively infinite reservoir relative to the capacity of the discharge products, meaning that deviations above 100% coulombic efficiency are not unexpected for a constant voltage cutoff—discharge capacities on any given cycle are not directly limited by the amount of Li recovered on the preceding charge step. However, as this occurs over repeated cycles, we hypothesize that "stranded" populations of discharge product can merge and allow for conductivity across the electrolyte surface upon further cycling, leading to more balance in the rates of production and recovery of this material. To gain more insight into these possible processes, we next analyze the voltage profile during cycling and attempt to corroborate polarization signatures with a combination of *operando* mass spectrometry and impedance spectroscopy.

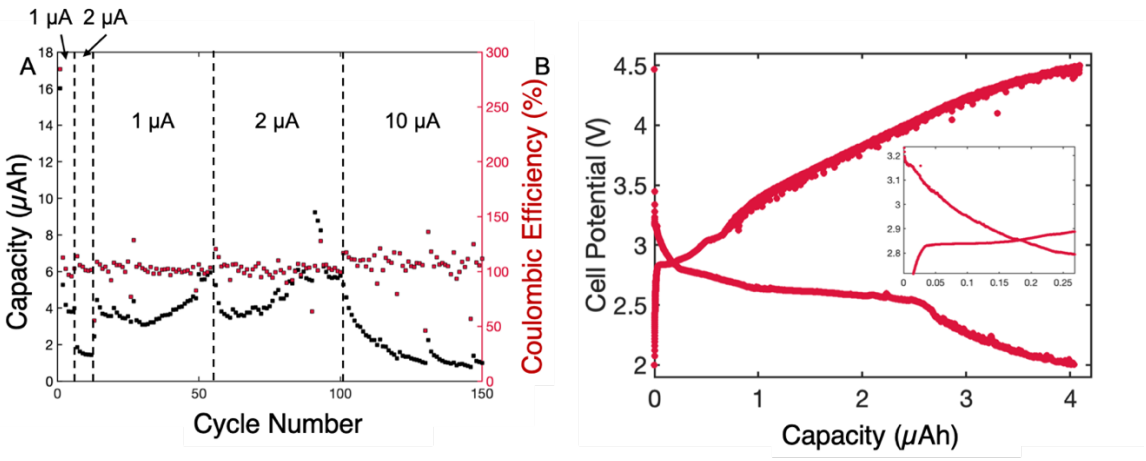

Figure 4. (A) Discharge capacity and coulombic efficiency for cell cycled at variable rates at 170˚C. (B) Voltage profile during continuous operation (cycle 14) at 170˚C at a cycle rate of 1 µA. Inset shows magnified region at beginning of charge/discharge.

3.2 Analysis of Polarization Features

The voltage profile of a cell, taken after reaching steady operation, is presented in **Figure 4B**. Several changes occur in the discharge curve relative to the initial cycle (**Figure 2B**), which contained significant break-in features from contaminants. In general, the stable cycling features become more consistent and defined. Notably, a defined plateau appears at ~2.6 V, followed by a decline to the designated cutoff at 2 V following this plateau. This behavior is consistent with the occurrence of "sudden death" once the discharge product has reached limiting dimensions. The plateau is likely associated with the formation of Li_2O_2 and/or Li_2O, which were identified by Raman spectroscopy and are in relative agreement with the standard reduction potentials to form these species given in Equations 1 and 2 above.[17] The steady decline toward cell death is also consistent with a plateau behavior manifested in cyclic voltammograms (CVs) shown in **Figure S1**. A sharp growth in current around 2.6 V in the cathodic (discharging) sweep transitions toward a more constant current characteristic with lower cell voltage. During this portion of the scan, a small peak on top of the flat feature is seen at 2.4 V, and this peak becomes more pronounced over

the course of early cycling (**Figure S1B-C**). A corresponding peak in the anodic (charging) sweep likewise emerges near 2.9 V, and we hypothesize that this pair of peaks relates to the establishment of well-defined phase domains of Li_2O_2 or Li_2O that are accessible to TPB regions.

Prior to the steady discharge at 2.6 V, a small capacity corresponding to about 0.2 μA-hr is observed above the expected equilibrium voltages for Li_2O_2 and Li_2O. While the high voltage associated with this feature cannot feasibly be generated by the reactions forming Li_2O_2 or Li_2O species, it could be consistent with the formation of a small amount of LiOH:[35]

$$3)\ 4\,Li^+ + 4e^- + 2H_2O + O_2 \rightarrow 4\,LiOH \quad (E^\circ = 3.45\ V)$$

LiOH is a known surface contaminant for LLZO, and the polishing and calcination steps in the synthesis are only actually established to remove Li_2CO_3 (even then imperfectly, as it slowly reforms under glovebox atmosphere).[36] We propose that the LLZO surface may have domains that cycle between LiOH and adsorbed water, and that these domains are increasingly accessed upon cycling. Association of capacity in this regime with LiOH is consistent with reports of cells operated with purposefully humidified O_2 in a similar configuration[21], where the OCV of the cell and therefore some capacity was found above 3 V. Direct observation of H_2O evolution during recharge will also be shown further below.

For the charging stage depicted in **Figure 4B**, two plateaus are also observed at 2.8V and 3.2 V. After these, we see a steady increase in cell potential up to the cutoff voltage of 4.5 V. The total capacity associated with the sum of the two charging plateaus does not align with the total capacity of the primary discharge process plateau at 2.6 V, suggesting there is an initially facile decomposition of a minor portion of the discharge products, followed by greater overpotential processes to complete the recharge. This would be consistent with the hypothesis that some

discharge product may be partially stranded and harder to decompose as we move to further into the charging regime.

3.3 Mass Spectrometry Analysis

To further probe the nature of the discharge products, EC-MS experiments were conducted while charging cells. Partial pressures of O_2, CO_2 , and H_2O were continuously monitored in the headspace of the cell to quantify their evolution in accordance with the decomposition of (mainly) Li_2O_2, Li_2O, and Li_2CO_3, with perhaps some other stoichiometries of products. As shown in **Figure 5**, evolution of gases is first detected at approximately 3.5V during charge, with O_2 being the dominant initial product. We note that an increased charging rate was necessary to achieve good resolution on the MS, and the associated iR-loss makes comparison of exact voltages to the galvanostatic cycling voltages above difficult. Nonetheless, qualitative features of the gas evolution are informative. In contrast to the O_2 signal, the CO_2 signal peaks at higher voltage. Evolution of a small quantity of CO_2 coincident with O_2 evolution suggests that the early traces of CO_2 correspond to decomposition of a small quantity of a carbonate-containing compound within the initial discharge product. The main source of CO_2 releases later and peaks near the maximum charging voltage, where O_2 is already nearly exhausted. However, there is a clear secondary peak shoulder in the O_2 signal—coincident with the CO_2 peak—suggesting that at a certain point the Li_xO_y discharge products are fully decomposed and further evolution of O_2 is due to Li_2CO_3 decomposition from the surface of the LLZO.[36] Using calibration gases, we calculated total evolution of each gas for one cycle to be 0.55 nanomols O_2 and 0.0115 nanomols CO_2 respectively. The total amount of O_2 evolved (minus ~0.006 nanomoles for the stoichiometric amount of O_2 associated with CO_2 evolution from Li_2CO_3) would correspond to a “uniform” Li_2O_2 discharge product thickness of ~450 nm, ignoring Au current collectors and assuming a conformal layer with

the bulk density of Li_2O_2. This estimate is only mentioned to serve as a point of reference, since (i) the charging current of this experiment is higher than that from earlier cycling, (ii) the product grows only near triple-phase boundaries, and (iii) there is also Li_2O present. Relative to the electrical points of contact (TPB regions), the thicknesses achieved are much greater, as was observed in the SEM imaging above. We again emphasize that the current demonstration has not been engineered to maximize capacity, and that more advanced approaches to fabricating current collectors—e.g. lithography—could be utilized to raise the nominal areal capacity of the cell significantly.

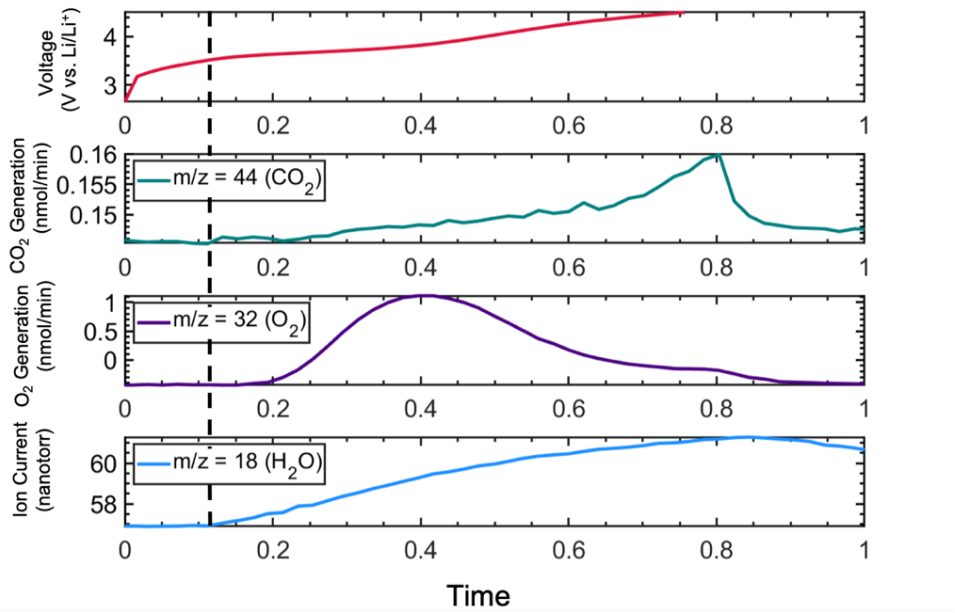

Figure 5. Evolution of O_2, CO_2 and H_2O as detected by EC-MS as correlated to charging voltage at an applied current of 30 μA.

Evolution of water was also detected during charging measurements (**Figure 5**, bottom). Its initial detection occurs with the same onset as O_2 (~3.5V), just above the standard potential for LiOH (Eq. 3). This suggests that we may be accessing some amount of LiOH during cycling, and that LLZO can retain water that only slowly desorbs from the surface. Alternatively, the CO_2 that evolves from the decomposition of any residual carbonate could react with LiOH, releasing H_2O

in the process.[37,38] Having stated this, the lack of an identifiable LiOH peak on the discharge product Raman spectra (**Figure** 3B) suggests that perhaps a less defined hydrated product, rather than pure crystalline LiOH, is involved. This species may relate to the unidentified peak at 675 cm^{-1}. The spectra of clean LLZO (**Figure 3B**) also did not have the 675 cm^{-1} peak we are ascribing to Li-hydroxides, further suggesting this peak is the result of electrochemical cycling.

3.4 Impedance Analysis

The evolution of the cell impedance is presented in a series of Nyquist plots at both charging and discharging cutoff voltages in **Figure 6A-B**. We call attention to the different scales in each case (order of magnitude larger impedances after charging), and we note that, with the high temperatures used in this study, the Li-LLZO interface and grain boundary impedances are too small to resolve from the cathode features,[39] permitting interpretation with the relatively simple circuits shown in the figure. Post-charge measurements should characterize the interface between Au and LLZO as well as any residual discharge products, while post-discharge measurements provide information about the main accessible product deposits. The high frequency intercept is related to the bulk LLZO resistance, while the semicircle following this intercept (only resolvable after discharge) is related to charge transfer at the cathode. The low frequency behavior after discharge is related to diffusion through the product film (mainly Li_2O_2) and can be interpreted as a Warburg diffusion process. After charging, we observe that the low frequency impedance behaves as a Warburg element with transmissive boundary, and notably with much larger resistance than is seen after discharge. In the absence of any Faradaic mechanisms, we would expect the Au-LLZO interface to exhibit blocking behavior; however, in light of our cycling measurements we expect that the resistive character is indicative of the stranded populations of discharge products proposed earlier. Essentially there is a wide distribution of time constants

associated with first decomposing the accessible products near the TPB regions, then breaking down additional material that is increasingly hard to access and does not fully decompose during charging. Thus the spectra were fit to the circuits shown in **Figure 6A** for charge and **6B** for charge. The cathode interface resistance (R_2) and diffusion components are plotted as a function of cycle number for charge (**Figure 6C**) and discharge (**Figure 6D**). The shrinking, in the discharge spectra, of the interface and diffusion impedances over time—most dramatically over early cycles—is

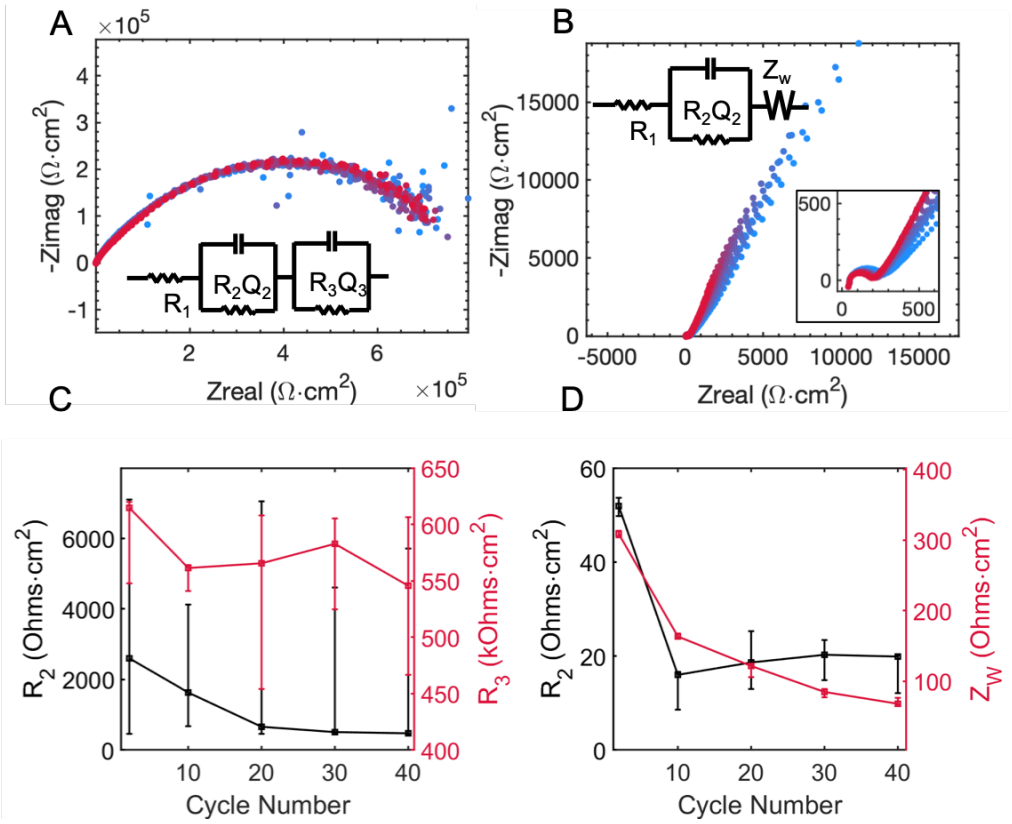

Figure 6. (A) EIS evolution as measured immediately post-charge (to 4.5 V) and (B) post-discharge (to 2 V). The first cycles are plotted in blue with a gradual transition to red (cycle 50). Frequency range is 1 MHz to 1 Hz. Equivalent circuits models are inset. Key impedance features (labeled in the insets) are plotted as a function of cycle number for (C) charge and (D) discharge, with error bars corresponding to 95% confidence intervals determined by Monte Carlo error sampling.

attributable to the growth of active/accessible area, in agreement with the increasing cycle capacity that was observed (**Figure 4A**) due to expansion of the product surface coverage. Deposition and recovery of the less-accessible product populations eventually approaches a balance between discharge and charge phases. These effects could likely be circumvented with finer current collector dimensions.

4. Conclusions

Cells with patterned Au cathodes were constructed to demonstrate the possible performance improvements for SSLO cells operating at elevated temperatures, enabled by thermal enhancement of the conductivities of discharge products. We found that these cells exhibit a stable long-term cycling performance at low current densities, however, higher current densities saw the capacity fade, due to charge transport limitations. Several materials characterization techniques were used in conjunction with quantified MS and cycling measurements to gain insight into the depth and composition of the discharge products present in these cells. Lithium oxides were identified as the primary discharge products, with a small amount of hydroxide and carbonates also present from brief atmospheric exposures. The persistence of hydroxide-related redox features with cycling suggests that water generated during decomposition of contaminants strongly adsorbs to LLZO and does not easily purge from the cell. The work more broadly suggests that, when coupled with further cell design to improve cathode active area, solid state Li-O_2 cells operating at high temperatures are a worthy of further investigation for Li-O_2 redox chemistry.

Supporting Information

Supporting Information contains: cyclic voltammetry under argon and oxygen at variable cycle age, cycling data for cells at 100°C, table of reference Raman peak assignments, and full EIS fitting data and methodology description.

Acknowledgements

This work was funded by NSF CBET #1806059. This research was supported in part by the Colorado Shared Instrumentation in Nanofabrication and Characterization Facility (COSINC-CHR), College of Engineering & Applied Science, University of Colorado Boulder.

Conflict of Interest

The authors declare no competing interests.

References

1. Girishkumar, G., McCloskey, B., Luntz, A. C., Swanson, S. & Wilcke, W. Lithium-air battery: Promise and challenges. *J. Phys. Chem. Lett.* **1,** 2193–2203 (2010).
2. Bruce, P. G., Freunberger, S. A., Hardwick, L. J. & Tarascon, J.-M. Li–O2 and Li–S batteries with high energy storage. *Nat. Mater.* **11,** 172–172 (2011).
3. Knudsen, K. B., Luntz, A. C., Jensen, S. H., Vegge, T. & Hjelm, J. Redox Probing Study of the Potential Dependence of Charge Transport Through Li2O2. *J. Phys. Chem. C* **119,** 28292–28299 (2015).
4. Luntz, A. C., Viswanathan, V., Voss, J., Varley, J. B., Nørskov, J. K., Scheffler, R. & Speidel, A. Tunneling and polaron charge transport through Li2O2 in Li-O2 batteries. *J. Phys. Chem. Lett.* **4,** 3494–3499 (2013).
5. McCloskey, B. D., Bethune, D. S., Shelby, R. M., Mori, T., Scheffler, R., Speidel, a, Sherwood, M. & Luntz, a C. Limitations in Rechargeability of Li-O2Batteries and Possible Origins. *J. Phys. Chem. Lett.* **3,** 3043–3047 (2012).
6. McCloskey, B. D., Speidel, A., Scheffler, R., Miller, D. C., Viswanathan, V., Hummelshøj, J. S., Nørskov, J. K. & Luntz, a. C. Twin problems of interfacial carbonate formation in nonaqueous Li-O2 batteries. *J. Phys. Chem. Lett.* **3,** 997–1001 (2012).
7. Mahne, N., Schafzahl, B., Leypold, C., Leypold, M., Grumm, S., Leitgeb, A.,

Strohmeier, G. A., Wilkening, M., Fontaine, O., Kramer, D., Slugovc, C., Borisov, S. M. & Freunberger, S. A. Singlet oxygen generation as a major cause for parasitic reactions during cycling of aprotic lithium–oxygen batteries. *Nat. Energy* **2,** 17036 (2017).

8. Yao, X., Dong, Q., Cheng, Q. & Wang, D. Why Do Lithium-Oxygen Batteries Fail: Parasitic Chemical Reactions and Their Synergistic Effect. *Angew. Chemie Int. Ed.* 2–12 (2016). doi:10.1002/anie.201601783
9. Johnson, L., Li, C., Liu, Z., Chen, Y., Freunberger, S. A., Ashok, P. C., Praveen, B. B., Dholakia, K., Tarascon, J. M. & Bruce, P. G. The role of LiO2 solubility in O2 reduction in aprotic solvents and its consequences for Li-O2 batteries. *Nat. Chem.* **6,** 1091–1099 (2014).
10. Viswanathan, V., Thygesen, K. S., Hummelshøj, J. S., Nørskov, J. K., Girishkumar, G., McCloskey, B. D. & Luntz, a C. Electrical conductivity in Li2O2 and its role in determining capacity limitations in non-aqueous Li-O2 batteries. *J. Chem. Phys.* **135,** 214704 (2011).
11. Radin, M. D., Monroe, C. W. & Siegel, D. J. Impact of Space-Charge Layers on Sudden Death in Li/O 2 Batteries. *J. Phys. Chem. Lett.* 3017–3022 (2015). doi:10.1021/acs.jpclett.5b01015
12. Gao, X., Chen, Y., Johnson, L. & Bruce, P. G. Promoting solution phase discharge in Li–O2 batteries containing weakly solvating electrolyte solutions. *Nat. Mater.* **15,** 918–918 (2016).
13. Knudsen, K. B., Vegge, T., McCloskey, B. D. & Hjelm, J. An Electrochemical Impedance Spectroscopy Study on the Effects of the Surface- and Solution-Based Mechanisms in Li-O $_2$ Cells. *J. Electrochem. Soc.* **163,** A2065–A2071 (2016).
14. Aetukuri, N. B., McCloskey, B. D., García, J. M., Krupp, L. E., Viswanathan, V. & Luntz, A. C. Solvating additives drive solution-mediated electrochemistry and enhance toroid growth in non-aqueous Li–O2 batteries. *Nat. Chem.* **7,** 50–56 (2015).
15. Giordani, V., Tozier, D., Tan, H., Burke, C. M., Gallant, B. M., Uddin, J., Greer, J. R., McCloskey, B. D., Chase, G. V. & Addison, D. A Molten Salt Lithium-Oxygen

Battery. *J. Am. Chem. Soc.* **138,** 2656–2663 (2016).

16. Khetan, A., Luntz, A. & Viswanathan, V. Trade-offs in capacity and rechargeability in nonaqueous Li-O2 batteries: Solution-driven growth versus nucleophilic stability. *J. Phys. Chem. Lett.* **6,** 1254–1259 (2015).
17. Xia, C., Kwok, C. Y. & Nazar, L. F. A high-energy-density lithium-oxygen battery based on a reversible four-electron conversion to lithium oxide. *Science.* **361,** 777–781 (2018).
18. Giordani, V., Tozier, D., Uddin, J., Tan, H., Gallant, B. M., McCloskey, B. D., Greer, J. R., Chase, G. V. & Addison, D. Rechargeable-battery chemistry based on lithium oxide growth through nitrate anion redox. *Nat. Chem.* **11,** (2019).
19. Kitaura, H. & Zhou, H. All-solid-state lithium-oxygen battery with high safety in wide ambient temperature range. *Sci. Rep.* **5,** 1–8 (2015).
20. Sun, J., Zhao, N., Li, Y., Guo, X., Feng, X., Liu, X., Liu, Z., Cui, G., Zheng, H., Gu, L. & Li, H. A Rechargeable Li-Air Fuel Cell Battery Based on Garnet Solid Electrolytes. *Sci. Rep.* **7,** 41217 (2017).
21. Suzuki, Y., Watanabe, K., Sakuma, S. & Imanishi, N. Electrochemical performance of an all-solid-state lithium-oxygen battery under humidified oxygen. *Solid State Ionics* **289,** 72–76 (2016).
22. Suzuki, Y., Kami, K., Watanabe, K. & Imanishi, N. Characteristics of discharge products in all-solid-state Li-air batteries. *Solid State Ionics* **278,** 222–227 (2015).
23. Lu, Y.-C., Crumlin, E. J., Veith, G. M., Harding, J. R., Mutoro, E., Baggetto, L., Dudney, N. J., Liu, Z. & Shao-Horn, Y. In Situ Ambient Pressure X-ray Photoelectron Spectroscopy Studies of Lithium-Oxygen Redox Reactions. *Sci. Rep.* **2,** 715 (2012).
24. Gerbig, O., Merkle, R. & Maier, J. Electron and ion transport in Li2O2. *Adv. Mater.* **25,** 3129–3133 (2013).
25. Lorger, S., Usiskin, R. & Maier, J. Transport and Charge Carrier Chemistry in Lithium Oxide. *J. Electrochem. Soc.* **166,** A2215–A2220 (2019).
26. Zhang, Y., Cui, Q., Zhang, X., McKee, W. C., Xu, Y., Ling, S., Li, H., Zhong, G.,

Yang, Y. & Peng, Z. Amorphous Li2O2: Chemical Synthesis and Electrochemical Properties. *Angew. Chemie - Int. Ed.* **55,** 10717–10721 (2016).

27. Radin, M. D. & Siegel, D. J. Charge transport in lithium peroxide: relevance for rechargeable metal–air batteries. *Energy Environ. Sci.* **6,** 2370–2379 (2013).
28. Tian, F., Radin, M. D. & Siegel, D. J. Enhanced charge transport in amorphous Li2O2. *Chem. Mater.* **26,** 2952–2959 (2014).
29. Huang, X., Xiu, T., Badding, M. E. & Wen, Z. Two-step sintering strategy to prepare dense Li-Garnet electrolyte ceramics with high Li + conductivity. *Ceram. Int.* (2017). doi:10.1016/j.ceramint.2017.12.217
30. Sharafi, A., Yu, S., Naguib, M., Lee, M., Ma, C., Meyer, H. M., Nanda, J., Chi, M., Siegel, D. J. & Sakamoto, J. Impact of air exposure and surface chemistry on Li–Li $_7$ La $_3$ Zr $_2$ O $_{12}$ interfacial resistance. *J. Mater. Chem. A* **5,** 13475–13487 (2017).
31. Bach, P., Stratmann, M., Valencia-Jaime, I., Romero, A. H. & Renner, F. U. Lithiation and delithiation mechanisms of gold thin film model anodes for lithium ion batteries: Electrochemical characterization. *Electrochim. Acta* **164,** 81–89 (2015).
32. Kwak, W. J., Park, J. B., Jung, H. G. & Sun, Y. K. Controversial Topics on Lithium Superoxide in Li-O2 Batteries. *ACS Energy Lett.* **2,** 2756–2760 (2017).
33. Halder, A., Wang, H.-H., Lau, K. C., Assary, R. S., Lu, J., Vajda, S., Amine, K. & Curtiss, L. A. Identification and Implications of Lithium Superoxide in Li–O $_2$ Batteries. *ACS Energy Lett.* 1105–1109 (2018). doi:10.1021/acsenergylett.8b00385
34. Gittleson, F. S., Yao, K. P. C., Kwabi, D. G., Sayed, S. Y., Ryu, W. H., Shao-Horn, Y. & Taylor, A. D. Raman Spectroscopy in Lithium-Oxygen Battery Systems. *ChemElectroChem* **2,** 1446–1457 (2015).
35. Burke, C. M., Black, R., Kochetkov, I. R., Giordani, V., Addison, D., Nazar, L. F. & McCloskey, B. D. Implications of 4 e $^-$ Oxygen Reduction via Iodide Redox Mediation in Li–O2 Batteries. *ACS Energy Lett.* 747–756 (2016). doi:10.1021/acsenergylett.6b00328
36. Delluva, A. A., Kulberg-savercool, J. & Holewinski, A. Decomposition of Trace Li

2 CO 3 During Charging Leads to Cathode Interface Degradation with the Solid Electrolyte LLZO. doi:10.1002/adfm.202103716

37. Kaufman, L. A. & McCloskey, B. D. Surface Lithium Carbonate Influences Electrolyte Degradation via Reactive Oxygen Attack in Lithium-Excess Cathode Materials. *Chem. Mater.* **33,** 4170–4176 (2021).
38. Williams, D. D. & Miller, R. R. Effect of Water Vapor on the LiOH-CO2 Reaction Dynamic Isothermal System. *Ind. Eng. Chem. Fundam.* **9,** 454–457 (1970).
39. Delluva, A. A., Dudoff, J., Teeter, G. & Holewinski, A. Cathode Interface Compatibility of Amorphous LiMn2O4(LMO) and Li7La3Zr2O12(LLZO) Characterized with Thin-Film Solid-State Electrochemical Cells. *ACS Appl. Mater. Interfaces* **12,** 24992–24999 (2020).